Journal of Materials Chemistry B

ROYAL SOCIETY OF CHEMISTRY

PAPER

View Article Online
View Journal | View Issue

Cite this: J. Mater. Chem. B, 2023, 11, 3836

Amplification of oxidative stress with a hyperthermia-enhanced chemodynamic process and MTH1 inhibition for sequential tumor nanocatalytic therapy†

Qingcheng Song,‡[ab] Yiran Zhang,‡[c] Xiangtian Deng,‡[d] Haiyue Zhao,[c] Yueyao Zhang,[ab] Junyong Li,[e] Wei Chen,*[ab] Hongzhi Hu*[f] and Yingze Zhang *[ab]

Received 8th December 2022,
Accepted 13th March 2023

DOI: 10.1039/d2tb02673b

rsc.li/materials-b

During chemodynamic therapy (CDT), tumor cells can adapt to hydroxyl radical (•OH) invasion by activating DNA damage repairing mechanisms such as initiating mutt homologue 1 (MTH1) to mitigate oxidation-induced DNA lesions. Therefore, a novel sequential nano-catalytic platform MCTP-FA was developed in which ultrasmall cerium oxide nanoparticle (CeO_2 NP) decorated dendritic mesoporous silica NPs (DMSN NPs) were used as the core, and after encapsulation of MTH1 inhibitor TH588, folic acid-functionalized polydopamine (PDA) was coated on the periphery. Once endocytosed into the tumor, CeO_2 with multivalent elements ($Ce^{3+/4+}$) could transform H_2O_2 into highly toxic •OH through a Fenton-like reaction to attack DNA as well as eliminating GSH through a redox reaction to amplify oxidative damage. Meanwhile, controllable release of TH588 hindered the MTH1-mediated damage repair process, further aggravating the oxidative damage of DNA. Thanks to the excellent photothermal performance of the PDA shell in the near-infrared (NIR) region, photothermal therapy (PTT) further improved the catalytic activity of $Ce^{3+/4+}$. The therapeutic strategy of combining PTT, CDT, GSH-consumption and TH588-mediated amplification of DNA damage endows MCTP-FA with powerful tumor inhibition efficacy both *in vitro* and *in vivo*.

1. Introduction

Chemodynamic therapy (CDT) has become a promising paradigm for tumor-specific therapy, which is based on the principle of transforming *in situ* overexpressed H_2O_2 in tumor cells into highly toxic •OH under catalysis with the Fenton reagent.[1–3] In this case, biological macromolecules such as DNA in tumor cells are vulnerable to •OH invasion, eventually leading to cell apoptosis.[4] However, several non-negligible obstacles make it difficult for CDT to achieve satisfactory efficacy. Firstly, the presence of antioxidant molecules such as GSH could scavenge •OH in time during CDT.[5–7] Secondly, the extensive existence of DNA damage repair systems within tumor cells such as mismatch repair (MMR) and base excision repair (BER) pathways could reduce oxidation-induced DNA lesions and thus significantly attenuate •OH-mediated oxidative therapy. Therefore, the development of an efficient sequential nano-catalytic therapy based on GSH consumption as well as the inhibition of DNA damage repair pathways is crucial to fully exploit the efficacy of CDT.

Recently, various metal ions (Fe^{2+}, Mn^{2+}, Cu^{+}, Cr^{4+}, and V^{2+}) were found to have excellent Fenton/Fenton-like catalytic activity.[8–10] The presence of mixed valence Ce^{3+} and Ce^{4+} endows CeO_2 NPs with a desirable catalytic performance for various applications.[11] Endogenous H_2O_2 could be converted into •OH for CDT by means of Ce^{3+}-dependent peroxidase-mimic (POD-mimic) activity.[12] Although ultrasmall CeO_2 nanozymes exhibit excellent enzyme-mimic catalytic performances, they are vulnerable to aggregation, which is induced by the significant increase in the surface free energy of CeO_2 as the particle size becomes smaller. It is well known that the particle size of CeO_2 has a significant impact on

[a] Department of Orthopaedic Surgery, Third Hospital of Hebei Medical University, Shijiazhuang, 050051, Hebei, P. R. China. E-mail: yzling_liu@163.com, dacheng1309@163.com; Tel: +86 18533112888, +8615333213911
[b] Orthopaedic Institution of Hebei Province, Shijiazhuang 050051, Hebei, China. E-mail: drchenwei2021@163.com; Tel: +86 18533112839
[c] School of Medicine, Nankai University, Tianjin, 300071, China. E-mail: zhangyiran1220@pku.edu.cn; Tel: +86 13521668185
[d] Trauma Medical Center, Department of Orthopedics surgery, West China Hospital, Sichuan University, Chengdu 610041, China. E-mail: 350144946@qq.com; Tel: +86 18683020107
[e] The People's Hospital, Shijiazhuang, 050051, Hebei, P. R. China
[f] Department of Orthopedics, Union Hospital, Tongji Medical College, Huazhong University of Science and Technology, Wuhan 430022, China. E-mail: 13720105746@163.com; Tel: +86 13720105746

† Electronic supplementary information (ESI) available. See DOI: https://doi.org/10.1039/d2tb02673b

‡ Equally contributed: Qingcheng Song, Yiran Zhang and Xiangtian Deng.

its catalytic performance, and the occurrence of inappropriate aggregation will undoubtedly lead to the weakening of enzymatic activity.[13,14] To overcome this obstacle, it is feasible to achieve a high degree of catalytic site dispersion by using the unique large mesoporous channels of DMSN as the deposition matrices. In particular, DMSN-based nano-systems have been demonstrated to be biocompatible *in vitro* and *in vivo*.[15,16] Therefore, DMSN could be considered as one of the promising catalyst supports in the field of biomedicine.

As the most toxic reactive oxygen species (ROS), •OH cannot be underestimated in terms of DNA damage.[17,18] Increased intracellular •OH tension could lead to oxidation of the deoxynucleoside triphosphate (dNTP) pool, in which guanine has the lowest reduction potential and becomes the primary site for •OH to attack DNA.[19] In this process, the final product 8-oxo-7,8-dihydroguanine (8-oxoG), as a common oxidized form of guanine base, could trigger programmed cell death by mismatching with original bases (usually with cytosine or adenine) during DNA replication.[20,21] As a defensive protein, MTH1 can sanitize the dNTP pool by hydrolyzing 8-oxodeoxyguanosinetriphosphate (8-oxodGTP) to pyrophosphate and 8-oxo-2′-deoxyguanosine monophosphate, thus guaranteeing that oxidized nucleotides are no longer recognized by DNA polymerase and avoiding base mispairing during replication.[22] Therefore, the existence of a DNA damage repairing mechanism in tumors presents a serious challenge to the ability of •OH to attack DNA. Recently, many MTH1 inhibitors have been reported to be able to effectively bind the active site of MTH1 protein, resulting in a large accumulation of 8-oxodG in dNTP pools.[23,24] Therefore, it is reasonable to believe that the addition of MTH1 inhibitor TH588 could further amplify the killing cell behavior following Fenton-like reaction.

In order to optimize the efficacy of tumor catalytic therapy, another feasible strategy could be introduced to improve the catalytic activity of nanozymes. Recently, growing evidence has indicated that temperature is one of the vital factors in improving Fenton reaction efficiency. Therefore, it is a promising strategy to introduce PTT into the nano-catalytic system to improve the catalytic performance of nanozymes. For instance, Dong *et al.* constructed bacteria-like PEG/Ce-Bi@DMSN nanozymes to achieve hyperthermia enhanced dual enzyme-mimic catalytic activity and glutathione consumption for efficient nano-catalysis of tumor therapy.[25] Additionally, $AgBiS_2$ hollow nanospheres with high photothermal conversion efficiency were developed to induce specific cytotoxicity by mimicking peroxidase.[26] Thanks to the intense absorption characteristics of polydopamine (PDA) in the NIR region of the spectrum, it could be used as a potential photothermal reagent for PTT – enhanced catalytic reaction. Surprisingly, as a mussel-inspired nanomaterial, PDA could form an adhesive film on the surface of various materials regardless of the surface shape.[27,28] Of note, PDA film is highly sensitive to acidic conditions, therefore, PDA coating could avoid the premature leakage of TH588 and exposure of the catalytic core during circulation in the blood.[29]

Herein, we fabricated a novel sequential nano-catalytic platform formed by CeO_2 NP decorated DMSN encapsulating MTH1 inhibitor TH588 and further coated with FA-functionalized PDA (DMSN-CeO_2@TH588@PDA-FA, abbreviated as MCTP-FA) (Scheme 1). The nanoplatform combined tumor targeting, tumor microenvironment (TME) responsive drug release, POD-mimic activity, GSH consumption, DNA damage repair system inhibition and PTT into a whole. Specifically, thanks to the excellent stability of the PDA shell at pH 7.4, premature release of TH588 into the blood circulation system was avoided. When MCTP-FA NPs accumulated in tumor tissue through an enhanced permeability and retention (EPR) effect and FA active targeting effect, the PDA shell could be cleaved at low pH to release TH588. Simultaneously, the redox reaction between

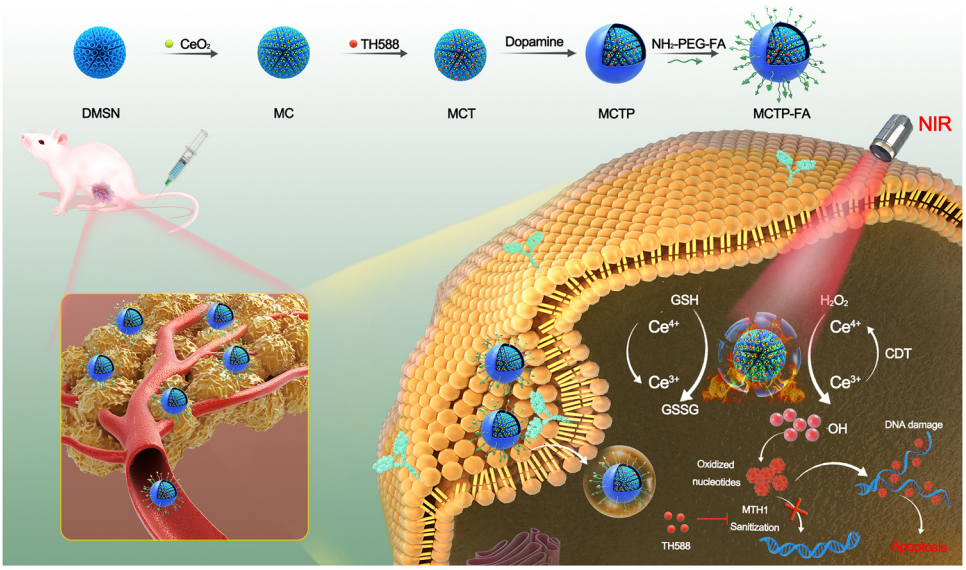

Scheme 1 Schematic illustration of the synthesis process of MCTP-FA NPs with hyperthermia-enhanced POD-mimic activity and GSH consumption for *in vivo* synergistic photothermal-enhanced nanocatalytic tumor therapy.

Ce^{4+} and GSH could alleviate the antioxidant capacity of tumor cells. Then, locally generated Ce^{3+} could react with H_2O_2 to produce $^{\bullet}OH$ to oxidize guanine, resulting in DNA mismatch. The released TH588 then inhibited the activity of MTH1 protein, thereby blocking the DNA damage repair pathway, leading to the accumulation of oxidative damage during CDT process. Furthermore, due to the satisfactory absorption of the PDA shell in the NIR region, the local high temperature induced by photon hyperthermia was utilized to significantly promote the activity of the POD-mimic as well as the GSH consumption. This hyperthermia-enhanced sequential catalytic therapy demonstrated superior antitumor efficacy both *in vitro* and *in vivo*.

2. Experimental procedure

2.1. Materials and cell lines

Tetramethyl-benzidine (TMB), *o*-phenylenediamine (OPD), 2-nitrobenzoic acid (DTNB), cetyltrimethylammonium bromide (CTAB), triethanolamine (TEA), citric acid, and cerium nitrate were purchased from Aladdin (Shanghai, China). Tetraethyl orthosilicate (TEOS), 2′,7′-dichlorodihydrofluorescein diacetate (DCFH-DA), folic acid (FA) and dopamine hydrochloride were purchased from Sigma-Aldrich (St. Louis, MO, USA). A calcein-AM/propidium iodide (PI) staining kit and an annexin V-FITC/PI apoptosis detection kit were obtained from Beyotime Biotechnology (China). All chemical reagents in this article were of analytical grade and were used without further purification.

Human OS cells (MNNG/HOS), bone marrow stromal cells (BMSCs), L929 fibroblast cells and human umbilical vein endothelial cell line cells (HUVEC cells) were obtained from the Cell Bank of Shanghai Institute of Biochemistry and Cell Biology, Chinese Academy of Sciences.

2.2. Synthesis of BMPA-CeO_2 NPs

CeO_2 NPs were synthesized using a simple aqueous method. Briefly, 2.5 g of cerium nitrate was dissolved in 100 mL of deionized (DI) water–ethylene glycol mixed solution (50/50 v/v). The temperature of the mixture was raised to 60 °C and then NH_4OH was introduced into the solution under intense agitation. After 6 h of continuous stirring, a yellow-colored colloidal solution was obtained, which was then centrifuged and washed with ethanol three times to obtain CeO_2 NPs. Subsequently, 0.5 g BMPA, 0.05 g citric acid and 15 mg of CeO_2 NPs were dissolved in 15 mL of chloroform–DMF mixed solution (50/50 v/v). After continuous stirring for 12 h, BMPA-CeO_2 NPs were obtained by centrifugation and dispersed in ethanol for later use.

2.3. Fabrication of MCT NPs

DMSN NPs were synthesized as previously described with slight modification.[30] Briefly, TEA (68 mg) was dissolved in 25 mL DI water at 80 °C. After magnetic stirring for 30 min, 84 mg NaSal and 380 mg CTAB were added to the reaction system and the mixture was stirred continuously for another 1 h. Then, 3.8 mL of TEOS was added dropwise into the reaction system under gentle stirring (~300 rpm), and the reaction was continued for 2 h. Furthermore, the mixture was centrifuged to collect the precipitate, followed by washing 3 times with water and ethanol to remove the residual reactants. The CTAB template was removed by re-dispersing the precipitates in 0.6 wt% ammonium nitrate (NH_4NO_3) ethanol solution and washed in ethanol under reflux three times (3 h per time). Finally, 100 μL APTES was added to DMSN ethanol solution and gently stirred at room temperature for 6 h. After centrifugation at 12 000 rpm for 15 min, DMSN-NH_2 was collected and re-suspended in ethanol for later use. Next, the prepared DMSN-NH_2 was added to 20 mL of BMPA-CeO_2 solution (5 mg mL^{-1}) and stirred at room temperature for 12 h to obtain DMSN-CeO_2 NPs (MC NPs).

For the loading of TH588, 75 mg MC NPs was dispersed in PBS solution (15 mL, pH 7.40). Afterwards, 8 mg of TH588 solution (20 mg mL^{-1}) was added to the above mixture and stirred overnight at room temperature. Then, the product was collected by centrifugation at 10 000 rpm for 10 min and gently washed with PBS three times before lyophilization. The concentration of TH588 in the supernatant was determined with a fluorescence spectrophotometer and the drug loading and encapsulation efficiencies were calculated according to the formula provided in the literature.[31]

2.4. Synthesis of MCTP-FA NPs

30 mg of MCT NPs was dispersed in 20 mL Tris buffer (pH 8.5, 10 mM) containing DA (20 mg) and stirred continuously at room temperature in the dark for 6 h. After stirring, the dark precipitate was collected by centrifugation and rinsed with DI water 3 times, then dried with lyophilization to obtain MCTP NPs.

For the modification of FA on the PDA surface, 20 mg MCTP and 20 mg NH_2-PEG-FA were added to 20 mL of Tris-HCl buffer (pH 8.5, 10 mM) and stirred for 10 h at room temperature. Next, the mixture was centrifuged at 12 000 rpm for 5 min to collect the precipitate and washed with DI water 3 times to remove the residual reactants. After lyophilization, the final product was denoted as MCTP-FA. The non-FA-functionalized MCTP was also synthesized in a similar way as described previously except that NH_2-PEG-FA was replaced by NH_2-PEG.

2.5. Characterization of MCTP-FA NPs

The morphology and size of NPs were recorded using transmission electron microscopy (TEM, JEOL 2100F, Japan). Dynamic light scattering (DLS) and zeta potential were determined using a Zetasizer (Zetasizer Advance, Malvern Instruments, UK). X-Ray photoelectron spectroscopy (XPS) spectra were obtained using a Thermo ESCALAB 250XI instrument to analyze the valence of the Ce component. The surface area and pore size distribution of the samples were determined using a Brunauer–Emmett–Teller (BET) method. The electron-spin-resonance (ESR) spectra of different reaction systems were obtained using a Bruker EMXplus spectrometer.

2.6. Evaluation of photothermal properties *in vitro*

The photothermal performances of DMSN and MCTP-FA NPs (200 μg mL^{-1}) *in vitro* were studied under 808 nm NIR irradiation with a laser power density of 1.0 W cm^{-2}. To detect the

influence of power density on the photothermal performance, an NIR laser with different power densities (0.5–2.0 W cm^{-2}) were used to irradiate MCTP-FA solution (100 μg mL^{-1}). Moreover, to examine the concentration-dependency of the photothermal effect, various concentrations of MCTP-FA NPs (50, 100 and 200 μg mL^{-1}) were irradiated using an 808 nm NIR laser with a power density of 1.0 W cm^{-2} for 10 min. To study the thermal stability of NPs, MCTP-FA solution was irradiated with a power density of 1.0 W cm^{-2} for five cycles, each consisting of a 5 min heating phase and natural cooling phase, and the temperature changes were recorded every 30 s.

In order to explore the photothermal conversion efficiency (η) of MCTP-FA NPs, the heating and natural cooling processes of MCTP-FA suspensions (200 μg mL^{-1}) under NIR irradiation (808 nm, 1.0 W cm^{-2}) were recorded, and the η was determined according to the following formula:

$$\eta = \frac{hS(T_{max} - T_{surr}) - Q_w}{I(1 - 10^{-A_\lambda})} \quad (1)$$

in which h represents the heat transfer coefficient, S represents the surface area of the container, T_{max} is the equilibrium temperature of the sample solution, and T_{surr} is the ambient temperature. I represents the power density of an 808 nm NIR laser. A_λ is the absorbance of sample solution at a wavelength of 808 nm. Q_w was obtained through the heating process of DI water irradiated with an NIR laser, and the formula is as follows:

$$Q_w = \frac{m_w C_w \Delta T_{max}}{\Delta t} \quad (2)$$

in which m_w is the mass of water, C_w is the specific heat capacity of water, ΔT_{max} is the temperature change of DI water irradiated using an NIR laser after reaching the equilibrium of the system, and Δt is the irradiation duration.

To calculate hS, the following formulas were introduced:

$$t = -\tau_s \ln \theta \quad (3)$$

$$hS = \frac{m_w C_w}{\tau_s} \quad (4)$$

in which τ_s is the time constant of the system, θ is the ratio between the real-time temperature difference in the cooling process of the system and the temperature difference in the equilibrium state.

2.7. Detection of the peroxidase-mimic activity of MC NPs and kinetic assay

TMB and OPD were utilized as the ROS probe to investigate the POD-mimic activity. In brief, TMB (30 mM, 20 μL), MC (100 μg mL^{-1}, 200 μL) and H_2O_2 (10 mM, 20 μL) were added to 2 mL PBS solution (pH 5.5) and reacted for 10 min. The absorbance at 652 nm was detected using a microplate reader to verify ROS generation. The steady-state kinetic assays were determined at different temperatures (25 °C, 50 °C) in 300 μL PBS solution (pH 5.5) containing MC NPs (100 μg mL^{-1}), H_2O_2, and TMB. The kinetic analysis of MC NPs was carried out with different concentrations of H_2O_2 (5, 10, 20, 40, 60, 80, 100 mM) as the substrate. The initial reaction velocity (v_0) of $^{\bullet}OH$ generation corresponding to each H_2O_2 concentration at 25 °C and 50 °C was calculated according to the Beer–Lambert law, and the formula is as follows:

$$A = \varepsilon l c \quad (5)$$

in which A is the absorbance, l is the thickness of the absorption layer and c is the concentration of the light-absorbing substance, and the extinction coefficient (ε) of oxTMB is 39 000 M^{-1} cm^{-1}. Then the reaction rate was plotted according to the corresponding H_2O_2 concentration, and Michaelis–Menten curve fitting was performed. Furthermore, a linear double reciprocal plot (Lineweaver–Burk equation) was used to determine the Michaelis–Menten constant (K_m) and maximum reaction velocity (V_{max}). The formula is as follows:

$$v_0 = \frac{V_{max} \cdot [S]}{K_m + [S]} \quad (6)$$

$$\frac{1}{v_0} = \frac{K_m}{V_{max}} \cdot \frac{1}{[S]} + \frac{1}{V_{max}} \quad (7)$$

2.8. Measurement of GSH elimination

To explore the GSH elimination properties of MC NPs, MC NPs (100 μg mL^{-1}) were added to PBS solution with GSH (10 mM) and co-incubated at 37 °C and 50 °C respectively. Subsequently, 0.3 mM DTNB solution was added to detect the content of GSH in the reaction system. The changes in absorbance at 412 nm after a certain reaction time were measured using a microplate analyzer.

2.9. Measurement of intracellular ATP levels

An ATP determination kit was used to assess the intracellular ATP content. In brief, MNNG/HOS cells were seeded into a 6 well plate (2.0 mL, 1.5 × 10^5 cells in each well), and the culture was continued for 24 h after receiving different treatments. Then, the cells were washed with PBS 3 times and lysed with lysis buffer at −4 °C. The supernatant was collected by 10 000 rpm centrifugation for 10 min and the ATP level was detected by using an ATP detection kit according to the manufacturer's protocol.

2.10. *In vitro* cellular uptake assay

Cell phagocytosis was detected using an inverted fluorescence microscope. The Ce6-labeled nanocomposites were prepared using the following method. The MC (10 mg) NPs were dispersed in 10 mL PBS solution (pH 7.4) containing Ce6 (5 mg) and gently stirred for 24 h in the dark. Then, the product was centrifuged at 10 000 rpm for 10 min followed by washing three times with PBS to remove the residual Ce6. The PDA coating and FA modification were carried out as described previously to obtain MCP/Ce6 and MCP-FA/Ce6 NPs. To investigate the NPs cellular uptake efficiency, MNNG/HOS cells were seeded in 6 well plates (1 × 10^5 cells per well) and incubated overnight at 37 °C. After complete adherence, the spent medium was replaced with fresh medium containing Ce6-labeled nanocomposites

(Ce6 = 10 μM) and cultured at 37 °C in a humidified atmosphere of 5% CO_2 for 4 h. For the competitive inhibition group, cells were pretreated with free FA (2 mM) before adding MCP-FA/Ce6 and cultured for 2 h under the same conditions. Subsequently, after washing carefully with PBS twice, the cells were incubated with Hoechst 33342 (10 μg mL^{-1}) for 20 min. Finally, the samples were rinsed with PBS and observed using a fluorescence microscope (Olympus Corporation, Tokyo, Japan).

2.11. Intracellular •OH generation detection

A DCFH-DA probe was utilized to detect the generation of intracellular •OH. MNNG/HOS cells were seeded into a 6 well plate (1×10^5 cells per well) and cultured at 37 °C for 12 h. Then, the spent medium was replaced with fresh MEM containing MP-FA NPs or MCP-FA NPs (100 μg mL^{-1}) and cultured for another 6 h. Next, the medium was replaced again, and the illumination group received laser irradiation at 808 nm with a power density of 1 W cm^{-2} for 10 min, followed by co-incubation with DCFH-DA (10 mM) for 20 min. Finally, after washing with cold PBS, a fluorescence microscope was used to observe intracellular ROS fluorescence. Moreover, mitochondrial superoxide generation was evaluated using Mitosox Red fluorescence staining based on the above grouping.

2.12. Mitochondrial membrane potential detection

MNNG/HOS cells were seeded into a 6-well plate at a density of 1×10^5 cells per well. Then, the cells were treated with the following 6 groups: (1) control, (2) NIR, (3) TH588 (3 μg mL^{-1}), (4) MCP-FA (100 μg mL^{-1}), (5) MCTP-FA (100 μg mL^{-1}), and (6) MCTP-FA + NIR (100 μg mL^{-1}). After incubation with different formulations for 6 h, the cells in group (6) were irradiated with an NIR laser (808 nm, 1 W cm^{-2}) for 10 min. The mitochondrial membrane depolarization was determined by JC-1 fluorescence staining according to the manufacturer's protocol. Subsequently, the cells were rinsed with PBS twice and incubated with DAPI for 10 min. The cells were then imaged using a fluorescence microscope.

2.13. *In vitro* cytotoxicity evaluation

MNNG/HOS cells were seeded into a 96 well plate (100 μL, 5×10^3 cells per well) and cultured overnight at 37 °C until completely adherence. Then, fresh culture medium containing various concentrations of nanocomposites (6.25, 12.5, 25, 50, and 100 μg mL^{-1}) was added to replace the spent medium. After further cultivation for 6 h, the illumination group received laser irradiation at 808 nm (1 W cm^{-2}) for 10 min and further incubated for 12 h. Finally, the supernatant was removed, followed by the addition of 100 μL medium containing 10% CCK8 solution. After incubation for another 2 h in the dark at 37 °C, the absorbance of each well at 450 nm was measured using a microplate reader.

2.14. Hemolysis assay

2.0 mL whole anticoagulant blood samples of healthy mice were collected and centrifuged at 3000 rpm for 5 min at 4 °C. Then, the upper serum was discarded, and the red blood cells (RBCs) were obtained by washing with PBS 3 times and were re-suspended in 2 mL PBS solution. Subsequently, 100 μL of RBC suspension was added into 900 μL of MCTP-FA PBS solutions with various concentrations (25, 50, 100, 200, 400, and 800 μg mL^{-1}). 100 μL of the RBC suspension was added to 900 μL PBS and DI water respectively as negative and positive controls. The mixed samples were incubated at 37 °C for 2 h followed by centrifugation at 3000 rpm at 4 °C for 5 min. The absorbance of the supernatant was measured at 570 nm using a microplate reader.

2.15. *In vivo* fluorescence imaging and biodistribution analysis

The tumor-bearing mouse model was constructed by subcutaneously inoculating MNNG/HOS cell suspension (200 μL, 1×10^7 cells mL^{-1}) into the right flanks of nude mice. After the tumor volumes reached 80–100 mm^3, the tumor-bearing mice were injected with Ce6-labeled NPs (200 μL 2 mg mL^{-1}) through the tail vein. At the given time points, tumor fluorescence imaging was performed *in vivo* by using a small animal imaging system (PerkinElmer, Caliper Life Sciences, MA, USA). At 24 h after injection, the mice were sacrificed, and the major organs and tumor tissues were collected for *ex vivo* imaging analysis.

2.16. *In vivo* antitumor effect

Female BALB/c nude mice (weight 15–19 g, age 4–6 weeks) were provided by Hebei Ex&lnvivo Biotechnology Co. Ltd (Shijiazhuang, China). All animal experiments were performed according to protocols approved by the Experimental Animal Ethics Committee of Hebei Ex&lnvivo Biotechnology Co., Ltd. When the tumor reached approximately 80–100 mm^3, the mice were randomly divided into 6 treatment groups: (1) control, (2) NIR, (3) TH588, (4) MCP-FA, (5) MCTP-FA, and (6) MCTP-FA + NIR. According to the therapeutic regimen, 200 μL of different formulations (10 mg kg^{-1}) were injected into the mice every four days through the tail vein. At 6 h after the injection, the sixth group was irradiated with an 808 nm laser (1.0 W cm^{-2}) for 10 min. The changes in body weights and tumor volumes of each group were monitored every two days. After 14 days of treatment, the mice were sacrificed, the major organs (heart, liver, spleen, lung, and kidneys) and tumor tissues were collected and fixed with 4% paraformaldehyde for subsequent experiments. Hematoxylin and eosin (H&E) staining was performed on sections of major organs and tumor tissues for histological observation. Meanwhile, the tumor tissues were stained with Ki67 and terminal deoxynucleotidyl transferase-mediated dUTP-digoxigenin nick-end labeling (TUNEL) staining to monitor the apoptotic response.

2.17. Statistical analysis

All experiments were repeated at least 3 times under the same experimental conditions, and the data obtained were recorded as the mean ± standard deviation (SD). Student's *t*-test and one-way ANOVA were used to analyze the statistical differences. Statistical significance was assumed at $P < 0.05$.

3. Results and discussion

3.1. Synthesis and characterization of MCTP-FA NPs

DMSN NPs with fascinating central-radial pore structures were synthesized based on the Stöber mechanism and sol–gel chemistry, which provided robust nano-supports for the deposition of small catalytic nanoparticles in the inner channels (Fig. 1a). As shown in Fig. 1b, the transmission electron microscope (TEM) image revealed that the as-constructed DMSN NPs were uniform and discrete in size, with circular and mesoporous structures, in which the black structure is the DMSN skeleton, and the light gray area between the skeletons is the mesoporous channel. The SEM images also confirmed the regular sphericity and highly monodisperse nature of DMSN (Fig. S1, ESI†). The average diameter of DMSN NPs under the TEM was about 78.1 ± 3.4 nm, however, the data were smaller than the results of dynamic light scattering (DLS) analysis which might be attributed to the existance of a hydration shell in the periphery of DMSN after dispersion in aqueous solution (Fig. S2, ESI†). The surface area and pore size of DMSN were determined to be 116.65 m^2 g^{-1} and 19.34 nm, respectively, according to the results of the N_2 adsorption–desorption isotherm, which confirmed this unique mesoporous structure is of great significance for the subsequent decoration of ultrasmall CeO_2 NPs and drug loading (Fig. S3, ESI†). Then, CeO_2 NPs with uniform size were fabricated using a simple aqueous method and further integrated into the large mesopores of DMSN NPs (Fig. 1c).

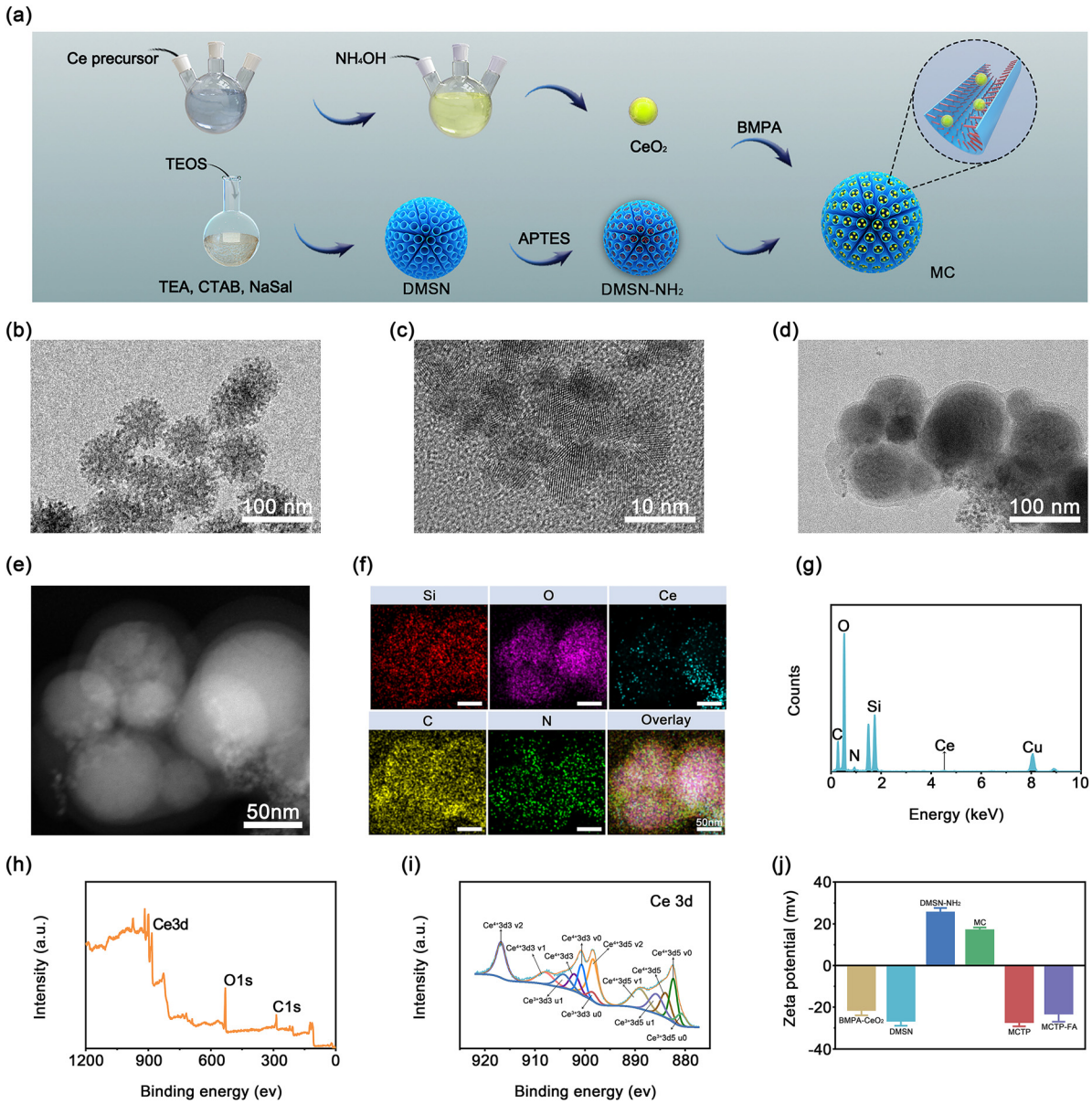

Fig. 1 (a) Schematic diagram for the fabrication of DMSN NPs and the deposition of CeO_2 NPs in DMSN mesoporous channels. TEM images of (b) DMSN NPs, (c) CeO_2 NPs, and (d) MCTP NPs. (e) Dark-field image and (f) the corresponding element mapping of MCTP NPs. (g) EDS spectrum of MCTP. (h) XPS survey spectra and (i) high resolution Ce 3d spectra of CeO_2 NPs. (j) Zeta potentials of samples at different synthetic steps.

The content of CeO_2 in DMSN-CeO_2 was about 11.64% detected by X-ray fluorescence (XRF) spectrometry. Subsequently, after the successful loading of TH588 into the mesopores of MC, the PDA shell was coated on the surface of the nanocomposites by means of oxidation self-polymerization according to the method described in previously published literature (Fig. S4, ESI†).[32] The distinct two-layer structure and more blurred mesoporous channels confirmed the successful grafting of PDA, and the average diameter of MCTP increased to 93.6 ± 6.5 nm (Fig. 1d). Furthermore, the HAADF image of MCTP and corresponding elemental mappings of Ce, Si, O, C and N also demonstrated the homogeneous distribution of CeO_2 in DMSN NPs and the successful coating of PDA shells (Fig. 1e and f). The EDS spectrum confirmed the coexistence of Ce, Si, O, C and N in MCTP NPs, which further demonstrated the successful preparation of the nano-system (Fig. 1g).

The existence of the Ce^{3+} and Ce^{4+} redox couple provided tremendous potential for Fenton-like and GSH consumption activities. Therefore, the mixed-valence of Ce was further investigated using the X-ray photoelectron spectroscopy (XPS) spectra of CeO_2. The XPS survey spectra showed that CeO_2 NPs contained Ce, C and O elements (Fig. 1h). The high-resolution spectra of Ce and other relevant elements in CeO_2 NPs are displayed in Fig. 1i and Fig. S5 (ESI†). The Ce 3d XPS spectrum in Fig. 1i exhibits eight peaks at 882.3, 883.9, 889.0, 898.3, 900.7, 902.1, 907.9, and 916.8 eV which can be attributed to Ce^{4+} ions, while the peaks at binding energies of 880.7, 885.7, 898.4, and 904.2 eV can be assigned to Ce^{3+} ions. These results confirmed that CeO_2 with a mixed valence state provided tremendous potential for POD-mimic activity and glutathione-consumption capability.

Furthermore, to avoid the undesirable aggregation of CeO_2 NPs, DMSN with a fascinating mesoporous structure was used as the deposition matrices to achieve a high degree of dispersion of CeO_2. Specifically, CeO_2 could be modified with BMPA and reacted with APTES functionalized DMSN through a nucleophilic substitution reaction, which could serve as a bridge to anchor CeO_2 in the mesoporous channels of DMSN to form MC NPs. As shown in Fig. 1j, the zeta potential of DMSN was −26.27 ± 2.71 mV and reversed to 25.34 ± 2.41 mV after modification of the amino group, which created a prerequisite for the integration of BMPA-CeO_2 as well as the subsequent loading of TH588. The step-wise changes in the zeta potential of MC (16.75 ± 1.63 mV), MCTP (−26.96 ± 2.30 mV) and MCTP-FA (−22.84 ± 4.17 mV) indicated the successful construction of the nano-system. More importantly, the prepared MCTP-FA could form homogeneous dispersions under a variety of physiological conditions. Even after incubation with PBS and serum for 5 days, the DLS and zeta potential of MCTP-FA showed no significant changes, confirming the superior stability of these NPs for biomedical applications (Fig. S6, ESI†).

3.2. Photothermal properties of MCTP-FA NPs

To evaluate the photothermal conversion performance of the MCTP-FA, the temperature changes of different preparations under 808 nm laser (1 W cm^{-2}) irradiation were recorded using an IR thermal imaging camera. As shown in Fig. 2b, after 10 min of laser irradiation, there was no obvious change in the temperature of DI water and DMSN. In marked contrast, the temperature of MCTP-FA rapidly increased to 52.5 °C, which intuitively reflected its desirable photothermal capacity. The η value of MCTP-FA was calculated to be 43.8% according to formula (1) (Fig. 2c and d). Subsequently, the photothermal conversion performance of MCTP-FA with different concentrations under laser irradiation (1.0 W cm^{-2}, 10 min) was investigated. As shown in Fig. 2e and f, the temperature of the DI water group did not change significantly after 10 min of irradiation. Meanwhile, the temperature of MCTP-FA suspensions with a series of concentration gradients increased rapidly, indicating that MCTP-FA had concentration- and time-dependent photothermal conversion properties. In addition, the photothermal efficiency of MCTP-FA NPs also exhibited a distinct laser power intensity-dependent manner (Fig. 2g). Furthermore, to detect the photothermal stability of MCTP-FA NPs, we monitored the temperature change of the MCTP-FA suspension after 5 cycles of ON/OFF irradiation. As shown in Fig. 2h, no obvious changes were observed in the temperature curves and peak shapes after five cycles of laser irradiation. In conclusion, these results demonstrate that MCTP-FA NPs with both a high photothermal conversion capacity and photothermal stability could be used as an effective photothermal agent for tumor treatment.

3.3. Drug loading and release

Targeted delivery of MTH1 inhibitor to the site of CDT occurrence could maximize the efficacy of this sequential nanocatalytic therapy. Therefore, a DMSN-based composite catalytic carrier (MC NPs) was developed to encapsulate TH588 to improve its solubility and targeting. Next, the absorbance of TH588 with different concentrations was measured, and the concentration–fluorescence intensity standard curve was drawn according to the results, as displayed in Fig. S7 (ESI†). The drug loading efficiency and the corresponding encapsulation efficiency of TH588 was calculated to be 5.03% and 77.02% respectively.

Considering the acid-responsive depolymerization of the PDA shell, the release behavior of TH588 from MCTP-FA was further evaluated under different pH conditions. As shown in Fig. 2i, under the condition of pH 7.4, the PDA shell tightly blocked the mesoporous DMSN, thus preventing the premature release of TH588. In contrast, the cumulative release of TH588 increased up to 69.2 ± 2.3% within 50 h at pH 5.5, which demonstrated that the release behavior of TH588 was pH-dependent. For NIR triggered release behavior, explosive release of TH588 can be observed at pH 5.5 after exposure to NIR irradiation with a cumulative release amount of 80.9 ± 2.0%. Under the same conditions, the release amount of TH588 also increased slightly at pH 7.4 as the cumulative release amount increased from 27.2 ± 2.3% to 38.6 ± 2.0%. The above results revealed that MCTP-FA could achieve the release of TH588 on demand through a pH and NIR stimulus-triggering mechanism, which is of great significance for reducing the damage of normal tissues.

3.4. Biocompatibility evaluation of NPs

The excellent biocompatibility is an indispensable prerequisite for the application of nanocomposites *in vivo*.[33] First, a

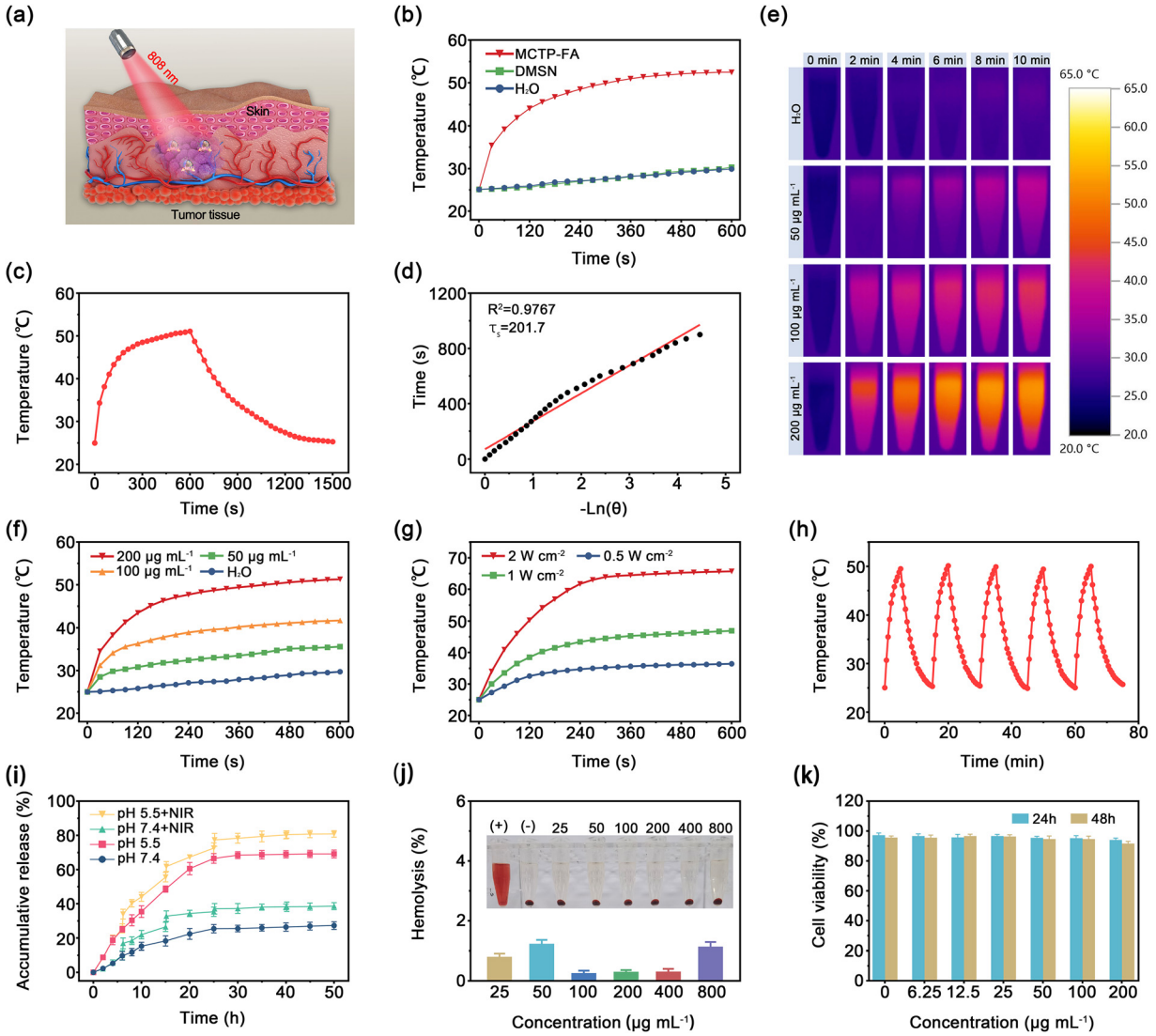

Fig. 2 (a) Schematic illustration of the photothermal effect of MCTP-FA NPs under 808 nm laser irradiation. (b) Temperature variation curves of DI water, DMSN and MCTP-FA solution under 808 nm laser (1.0 W cm^{-2}) irradiation. (c) Heating and cooling curve of MCTP-FA aqueous solution under 808 nm laser irradiation. (d) Linear fit of the time *versus* $-\ln\theta$ obtained from the cooling period of MCTP-FA solution. (e) Infrared thermal images of MCTP-FA aqueous solution with different concentrations under 808 nm laser (1.0 W cm^{-2}) irradiation. (f) Time-dependent temperature changes of MCTP-FA dispersion at elevated concentrations under 808 nm laser (1.0 W cm^{-2}) irradiation. (g) Time-dependent temperature changes of MCTP-FA dispersion under 808 nm laser irradiation with different power densities. (h) Heating/cooling profiles of the MCTP-FA aqueous solution after 808 nm laser (1.0 W cm^{-2}) irradiation for five laser on/off cycles. (i) TH588 release profiles of MCTP-FA at pH 7.4 and 5.5 with or without NIR irradiation (808 nm, 1.0 W cm^{-2}, 10 min). (j) Hemolysis assay of different concentrations of MCTP-FA samples. (k) Cell viabilities of BMSCs cells incubated with MCTP-FA NPs at a series of concentrations for 24 h and 48 h.

hemolysis assay was conducted to evaluate the blood compatibility of MCTP-FA. As shown in Fig. 2j, even when the concentration of MCTP-FA NPs reached 800 μg mL^{-1}, the hemolysis rate was still lower than 2%, confirming its good biocompatibility. Furthermore, the biocompatibility evaluation of MCTP-FA NPs was conducted on L929 fibroblast cells, human umbilical vein endothelial cell line cells (HUVEC cells) and bone marrow stromal cells (BMSCs) using a CCK8 assay. As shown in Fig. 2k and Fig. S8 (ESI†), MCTP-FA NPs exhibited no significant cytotoxicity even when the concentration reached 200 μg mL^{-1} after 48 h of incubation. All these results indicate that the prepared MCTP-FA NPs possessed excellent biocompatibility and biosafety as a nanocatalylic therapeutic platform for *in vivo* and *in vitro* therapy.

3.5. Evaluation of POD-mimic activity and GSH consumption

In our study, the •OH generation capacity of MC NPs was evaluated in detail. In consideration of the short lifetime and high chemical activity of •OH, a reliable electron spin resonance (ESR) spectrum by using DMPO as a specific trapping agent was utilized to detect and verify the •OH generation. As shown in Fig. S9 (ESI†), a more pronounced 1:2:2:1 •OH signal was observed at an elevated temperature under acid conditions, which strongly indicated that the hyperthermia facilitated the

ability of the MC NP-mediated Fenton-like reaction in the generation of •OH.

Furthermore, the POD-mimic activity of MC NPs was determined by a classical colorimetric reaction based on 3,3′,5,5′-tetramethyl-benzidine (TMB) and o-phenylenediamine (OPD). The detection principle is displayed in Fig. 3a, in the presence of H_2O_2, TMB can be oxidized by •OH generated in a Fenton reaction to produce blue-colored oxTMB with characteristic absorption peaks at 370 nm and 652 nm. Similar to TMB, OPD could also serve as an indicator of •OH and was oxidized to orange-colored oxOPD with characteristic absorption at 417 nm. Furthermore, considering the hyperthermia-enhanced Fenton-like catalytic performance in the ESR spectrum, the enzymatic activity of MC NPs was determined at temperatures ranging from 20 °C to 70 °C (Fig. S10, ESI†). We found that the optimum temperature for MC enzyme activity was about 57 °C which provided support for our subsequent quantitative analysis of hyperthermia-enhanced enzyme catalytic kinetics. A water bath with different temperatures was applied to simulate the different reaction system temperatures induced by MCTP-FA NPs with or without laser irradiation. As shown in Fig. 3b, the emergence of blue oxTMB could be observed when MC NPs were added to a mixture solution of H_2O_2 and TMB. However, an apparent blue-colored solution can be obtained with more pronounced characteristic absorption peaks at 370 nm and 652 nm at 50 °C, which confirmed that hyperthermia could enhance •OH generation by promoting the activity of MC NPs. A similar phenomenon was observed in the colorimetric analysis of OPD (Fig. 3c).

To further elucidate the POD-mimic catalytic activity of MC NPs, steady-state catalytic kinetics was determined with TMB and H_2O_2 (5, 10, 20, 40, 60, 80, and 100 mM) as substrates in an acidic environment. The absorbance variation at 652 nm of the reaction system with different concentrations of H_2O_2 were recorded in real time (Fig. 3d and f). Corresponding to each H_2O_2 concentration, the initial reaction rate (ν_0) of •OH generation was calculated using the Beer–Lambert law (eqn (5)) according to the variation of absorbance. Subsequently, we found that the reaction rates conformed to Michaelis–Menten behavior (eqn (6) and Fig. S11a, ESI†) in a particular range of substrate concentration.[34] Besides, the V_{max} and K_m of MC NPs at room temperature were determined using the linear double-reciprocal plot (eqn (7) and Fig. 3e), and were 2.27×10^{-8} M s^{-1} and 6.17 mM respectively.

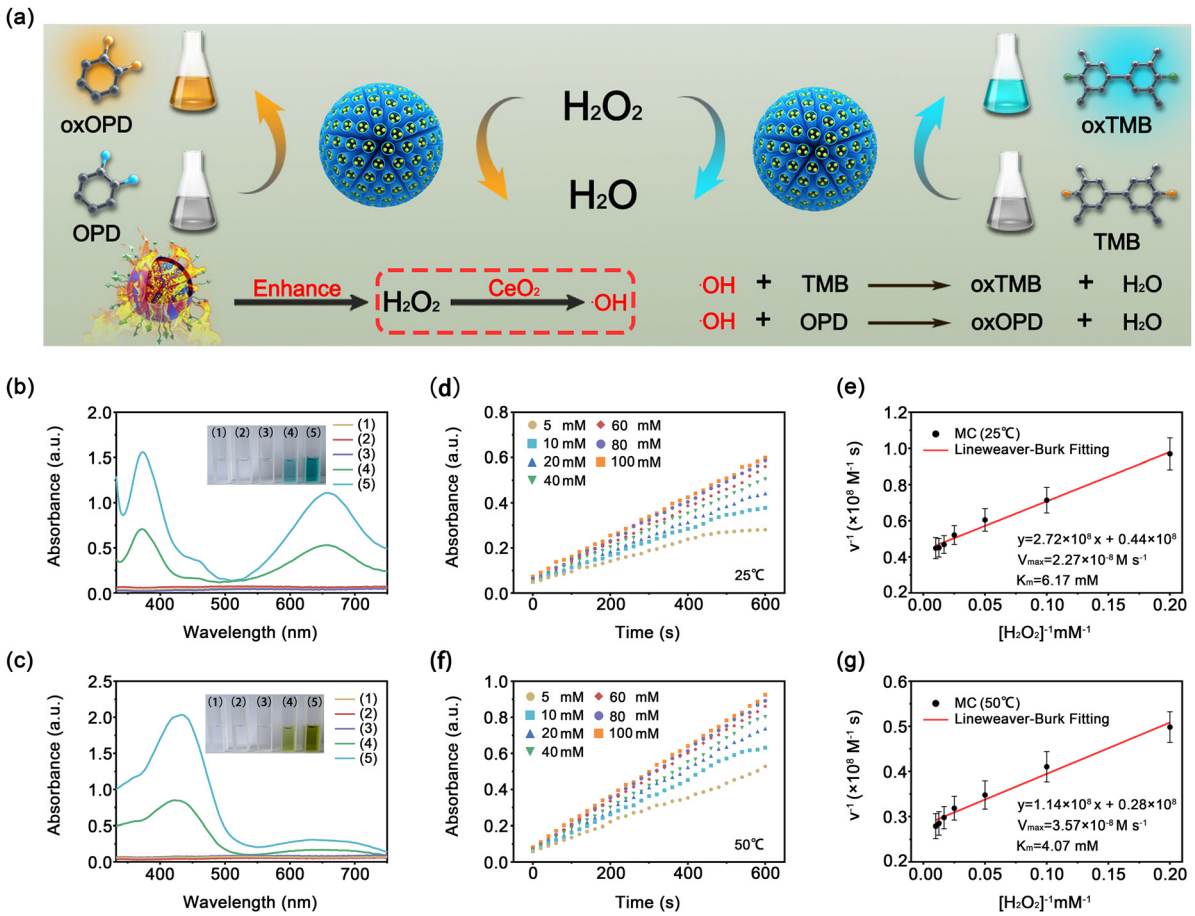

Fig. 3 (a) Schematic illustration of the POD-mimic catalytic process of MC NPs. (b and c) UV-vis absorption spectra and visual color changes of the catalyzed oxidation of TMB (oxTMB) (b) and OPD (oxOPD) (c) as catalyzed by: (1) PBS, (2) PBS + H_2O_2, (3) PBS + 50 °C, (4) PBS + MC + H_2O_2 + 25 °C, and (5) PBS + MC + H_2O_2 + 50 °C in an acidic environment (pH 5.5). The insets show the corresponding digital photos of each group. (d and f) Time-dependent absorbance changes at 652 nm as a result of the catalyzed oxidation of TMB at 25 °C (d) and 50 °C (f) with the addition of different H_2O_2 concentrations. (e and g) Lineweaver–Burk plotting for MC NPs with H_2O_2 as the substrate at 25 °C (e) and 50 °C (g).

Since the POD-mimic catalytic performance of MC NPs could be significantly promoted by hyperthermia, we further evaluated their catalytic activity at an elevated temperature. As expected, the catalytic activity of MC NPs was positively correlated with temperature and exhibited a higher absorbance intensity in the TMB-mediated chromogenic reaction. Similar to the above analysis process, the Michaelis–Menten fitting and linear double-reciprocal analysis on the ν_0 and the corresponding H_2O_2 concentration were also performed (Fig. S11b, ESI† and Fig. 3g). The V_{max} and K_m of MC NPs were calculated to be 3.57×10^{-8} M s^{-1} and 4.07 mM at 50 °C. As an evaluation index of the affinity of nanozyme to the substrate,[35,36] the K_m value decreased with the increase of temperature, indicating the higher affinity of MC NPs to H_2O_2 under a high temperature environment. As expected, the influence of high temperature on Fenton-like catalytic efficiency was also apparent with an increased V_{max} value under hyperthermia conditions. Furthermore, the natural enzyme horseradish peroxidase (HRP) was used as a control group to evaluate the catalytic activity of the prepared materials. As shown in Fig. S12 (ESI†), MC NPs exhibited a higher V_{max} and more ideal affinity toward H_2O_2 compared with HRP. Moreover, from the perspective of K_m and V_{max} as the evaluation criteria, the prepared Fenton catalytic core MC NPs exhibited more ideal POD-mimic catalytic efficiency than the reported nanozyme (Table S1, ESI†).

The high GSH concentration within tumor cells can scavenge •OH and further impair the efficacy of ROS-based therapy. Considering the hyperthermia enhanced POD-mimic catalytic activity, the effect of hyperthermia on GSH consumption was further evaluated. It could be seen that with the prolongation of the reaction time, the typical absorbance of DTNB (–SH indicator) at 412 nm gradually decreased, demonstrating the effective depletion of GSH by MC NPs. Moreover, the GSH depletion velocity at 50 °C was significantly faster than that at 37 °C, confirming the effect of hyperthermia on accelerating GSH consumption (Fig. S13a, ESI†). Encouraged by the hyperthermia-enhanced GSH consumption, we further investigated the effects of various formulations on intracellular GSH levels. As predicted, the cells treated with MCTP-FA + NIR exhibited a dramatic reduction in intracellular GSH level (Fig. S13b, ESI†). These results indicated that MCTP-FA could achieve extensive accumulation of •OH in tumor cells through hyperthermia-enhanced POD-mimic activity and GSH consumption.

3.6. Cellular uptake

Effective endocytosis of nanocomposites by tumor cells is a crucial initial step for the therapeutic effect of multifunctional nanozymes.[37] One feasible approach is to modify a targeted ligand on the periphery of the nanocomposites, which endows them with the ability to bind specifically to receptors overexpressed on the membrane of cancer cells.[38] Fortunately, thanks to the overexpression of FOLR in osteosarcoma cells, the conjugation of FA on the outer surface of PDA is expected to increase the aggregation of nanoparticles in tumor cells.[39] Ce6 with red fluorescence was used for intracellular localization of nanocomposites. As shown in Fig. 4a, after the cells were co-incubated with free Ce6 for 4 h, only weak red fluorescence was observed. In contrast, MCP/Ce6 exhibited an obvious red fluorescence signal, which may be attributed to the PDA shell-enhanced endocytosis. Notably, a higher red fluorescence signal was observed in the MCP-FA/Ce6 group than in the MCP/Ce6 group after 4 h of incubation. Furthermore, a competitive inhibition test of FA molecules was performed by pretreating cells with free FA molecules, in which a much weaker fluorescence signal was observed compared with the MCP-FA/Ce6 group, confirming the critical role of FA ligands in mediating nanocomposite endocytosis.

3.7. Cellular cytotoxicity of NPs *in vitro*

The *in vitro* cytotoxicity of MCTP-FA NPs on MNNG/HOS cells was evaluated by CCK8 assay. As shown in Fig. 4b, the viabilities of the MNNG/HOS cells treated with MCTP-FA + NIR exhibited an obvious concentration-dependent decrease, with an inhibition rate up to 87.3% at 100 μg mL^{-1}. Moreover, the cell inhibitory ability of MCTP-FA + NIR (IC_{50} = 3.16 μg mL^{-1}) was higher than that of the MCP-FA (IC_{50} = 11.66 μg mL^{-1}) and MCTP-FA (IC_{50} = 8.51 μg mL^{-1}) groups. These results demonstrated that photothermal enhanced sequential nanocatalytic therapy had a highly synergistic inhibitory effect on the proliferation of MNNG/HOS cells.

In order to further investigate the capability of MCTP-FA NPs in hyperthermia enhanced CDT efficiency, the intracellular generation of •OH was monitored by 2,7-dichlorofluorescein diacetate (DCFH-DA), which could react with ROS to form 2,7-dichlorofluorescein (DCF) with green fluorescence.[40] As shown in Fig. 4c, only negligible fluorescence appeared in the control group and NIR group, while in contrast, more obvious green fluorescence was observed in the MCP-FA treatment group, which confirmed the activity of the intracellular POD-mimic catalytic enzyme. Meanwhile, brighter green fluorescence was detected in the MCP-FA + NIR group than in the MCP-FA group, confirming that the photothermal effect could improve the •OH generation efficiency.

Intracellular ROS accumulation could activate oxidative injury of tumor cells by inducing mitochondrial dysfunction. Therefore, the generation of mitochondrial superoxide was determined by the method of Mitosox Red fluorescence staining. As shown in Fig. S14 (ESI†), the formation of abundant ROS in the MCP-FA + NIR treatment group was accompanied by massive accumulation of superoxide in mitochondria, as proved by the red fluorescence. Collectively, this photothermal enhanced sequential catalytic strategy possessed unique advantages in elevating intracellular ROS levels as well as inducing oxidative damage to mitochondria.

To more intuitively evaluate the cytotoxicity of this sequential treatment strategy, MNNG/HOS cells were co-stained with calcein-AM (green) and PI (red) (live/dead staining assay) after different treatments. As shown in Fig. 4d, significant green fluorescence was observed in the control group and the NIR group, indicating that illumination alone had a minimal killing effect on cells. Compared with the weak red fluorescence in the TH588 group, the MCP-FA group and the MCTP-FA group

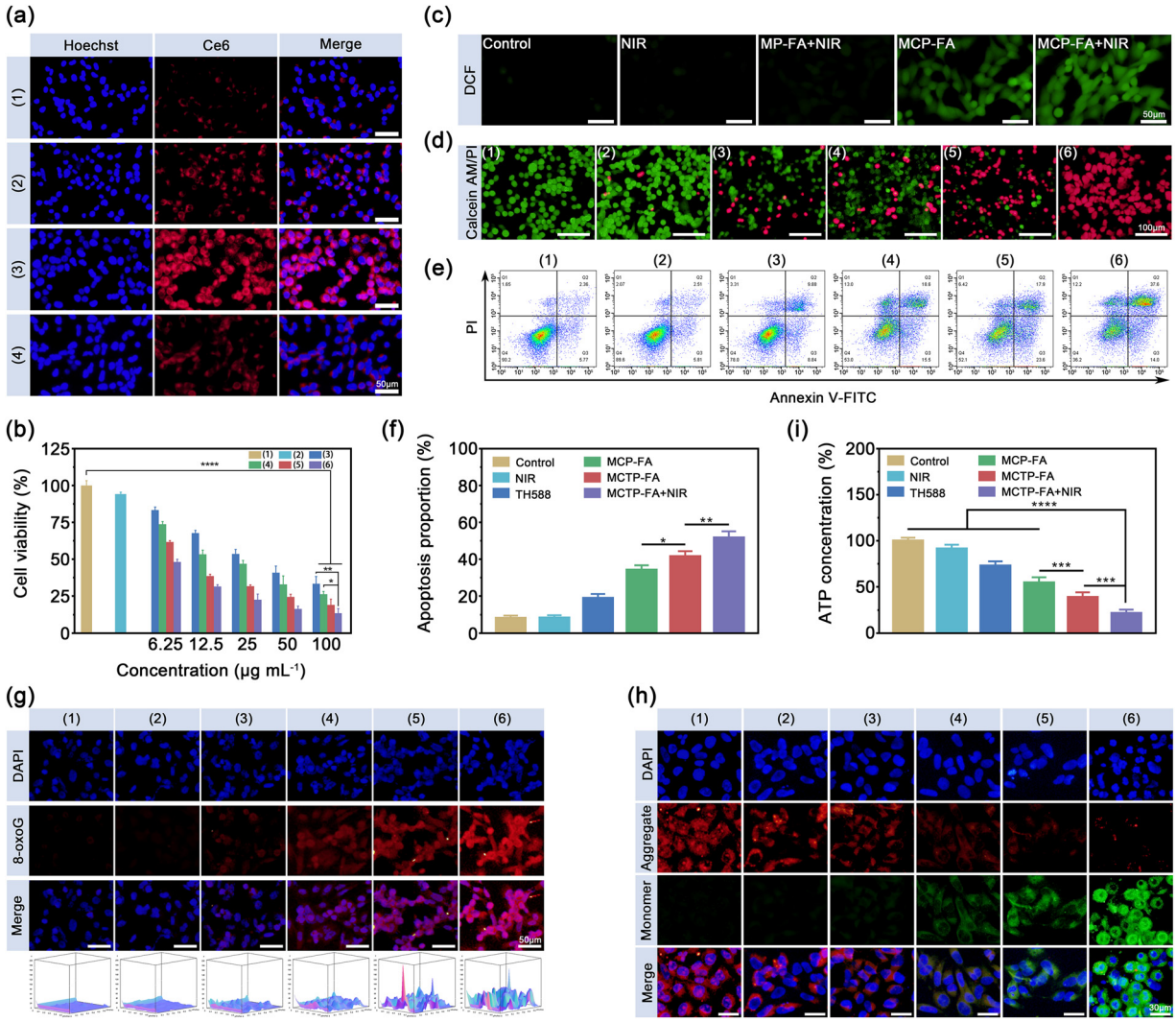

Fig. 4 (a) Fluorescence microscopy images of MNNG/HOS cells after incubation with (1) free Ce6, (2) MCP/Ce6, (3) MCP-FA/Ce6, and (4) MCP-FA/Ce6 + free FA for 4 h. (b) Cytotoxicity profiles of MNNG/HOS cells treated with: (1) control, (2) NIR, (3) TH588, (4) MCP-FA, (5) MCTP-FA, and (6) MCTP-FA + NIR. (c) Intracellular ROS levels after different treatments. (d) Calcein-AM/PI double staining, (e) annexin V-FITC/PI assay, (f) quantification of apoptosis ratios of MNNG/HOS cells, (g) immunofluorescence images of 8-oxoG and the corresponding surface plot images, and (h) JC-1 staining of MNNG/HOS cells after different treatments: (1) control, (2) NIR, (3) TH588, (4) MCP-FA, (5) MCTP-FA, and (6) MCTP-FA + NIR. (i) Intracellular ATP levels of MNNG/HOS cells after different treatments.

exhibited an increasingly strong red fluorescence signal, indicating that the combination of CDT with TH588-mediated DNA repair pathway inhibition is a promising anti-tumor approach. As expected, almost all cells died in the MCTP-FA + NIR group, confirming the indispensable effect of hyperthermia induced by the photothermal effect in promoting nano-catalytic therapy. Moreover, the apoptosis and necrosis of MNNG/HOS cells were quantitatively assessed by fluorescein-annexin V and propidium iodide (PI) assays. Consistently, it could be seen that MCTP-FA + NIR could induce a prominently higher level of cell apoptosis (Fig. 4e and f), demonstrating that this nanoplatform could offer an excellent antitumor effect *via* the apoptosis pathway.

3.8. Exploration of the mechanism in sequential catalytic therapy

Encouraged by the satisfactory cytotoxicity of this sequential therapy strategy, its antitumor mechanism was further investigated in detail. Guanine is the most susceptible DNA residue to $^{\bullet}OH$ oxidation due to its low reduction potential,[41] which could effectively lead to the formation of 8-hydroxy-7,8-dihydro-guanylradical (8-OHdG) which further transforms into 8-oxodG (Fig. S15, ESI†).[42,43] In order to intuitively demonstrate that this sequential catalytic treatment could induce more DNA mutants to accumulate in tumor cells, immunofluorescence staining was applied to detect the accumulation of 8-oxoG in cells after various treatments. As shown in Fig. 4g, the depletion of MTH1 as well as the enhancement of the POD-mimic effect under hyperthermia conditions could all lead to a large accumulation of 8-oxodG in cells, which could be confirmed by the obvious red fluorescence. Moreover, another specific DNA damage marker, 53BP1, was also used to measure the degree of DNA damage. As shown in Fig. S16 (ESI†), obvious 53BP1 foci in the nuclear region was observed in the MCP-FA

group, with further enrichment in the subsequent progressive treatment.

Intracellular ROS generation could induce mitochondrial dysfunction and ultimately trigger cell apoptosis.[44,45] Therefore, changes in mitochondrial membrane potential were determined by JC-1 assays to explore whether mitochondrial integrity was compromised after various treatments. As shown in Fig. 4h, the highest green-to-red fluorescence ratio was observed in the MCTP-FA + NIR group, indicating a dramatic reduction in mitochondrial membrane potential as well as more mitochondrial damage. Consistent with the results of JC-1 staining, quantitative analysis of mitochondrial membrane potential by JC-1 flow cytometry showed that MCTP-FA + NIR treatment could induce 29.6% mitochondrial damage (Fig. S17, ESI†).

As the energy factories of the cell, mitochondria are recognized as the vital source of ATP required to meet the various energy demands of the cell.[46] However, mitochondrial dysfunction can lead to the destruction of the oxidative respiratory chain, resulting in a decrease in the intratumoral ATP level, and it is then difficult to meet the needs of tumor proliferation.[47] Therefore, we further investigated the influence of sequential catalytic therapy on ATP levels in MNNG/HOS cells. As shown in Fig. 4i, intracellular ATP levels decreased tremendously in the MCTP-FA + NIR treatment group. Taken together, this sequential nano-catalytic treatment strategy can not only destroy the mitochondrial membrane potential, but also inhibit the generation of ATP in cells thus exhibiting an excellent antitumor efficiency.

3.9. Biodistribution and photothermal properties *in vivo*

The tumor-targeting ability and biodistribution of NPs *in vivo* were investigated using a fluorescence imaging experiment on the MNNG/HOS tumor-bearing mouse model. As shown in Fig. 5a, the fluorescence signal in the tumor region gradually increased over time and the strongest fluorescence signal was detected at 6 h post-injection, indicating the gradual accumulation and penetration process of the NPs in the tumor *via* the EPR effect and active targeting. In particular, a residual fluorescence signal could still be detected 24 h after injection. After 24 h of intravenous administration, the mice were sacrificed and tumor tissues and major organs were excised for semiquantitative mean fluorescence intensity (MFI) analysis. The results showed that the fluorescence signal in the tumor region was stronger than that in the major organs, further demonstrating the excellent tumor targeting, high uptake and retention ability of the nanocomposites (Fig. 5b and c).

Based on the observation of *in vivo* fluorescence imaging, the optimal time window for laser irradiation was determined to be 6 h after injection. We next evaluated the *in vivo* photothermal properties of MCTP-FA using an infrared thermal camera. As shown in the photothermal images (Fig. 5d) and time-temperature curves (Fig. 5e), the temperature in the PBS group only increased slightly after 10 min of NIR irradiation, while the temperature in the tumor region of the mice treated with MCTP-FA could reach about 50 °C, which is sufficient for the hyperthermia enhanced Fenton-like reaction.

3.10. *In vivo* synergistic therapy

Based on the above findings, we can speculate that the excellent therapeutic effect of MCTP-FA was mainly composed of two indispensable components: photothermal effect-triggered hyperthermia-augmented the •OH generation and the effective inhibition of the DNA damage repair mechanism. Inspired by the satisfying cytotoxicity results *in vitro*, we further evaluated the antitumor efficacy of MCTP-FA NPs using a MNNG/HOS tumor-bearing mice model. When the tumor volume reached about 80–100 mm^3, the tumor-bearing mice were randomly assigned into 6 groups: (1) control, (2) NIR, (3) TH588, (4) MCP-FA, (5) MCTP-FA, and (6) MCTP-FA + NIR. Next, the tumor-bearing mice were treated according to the procedure shown in Fig. 6a, and the

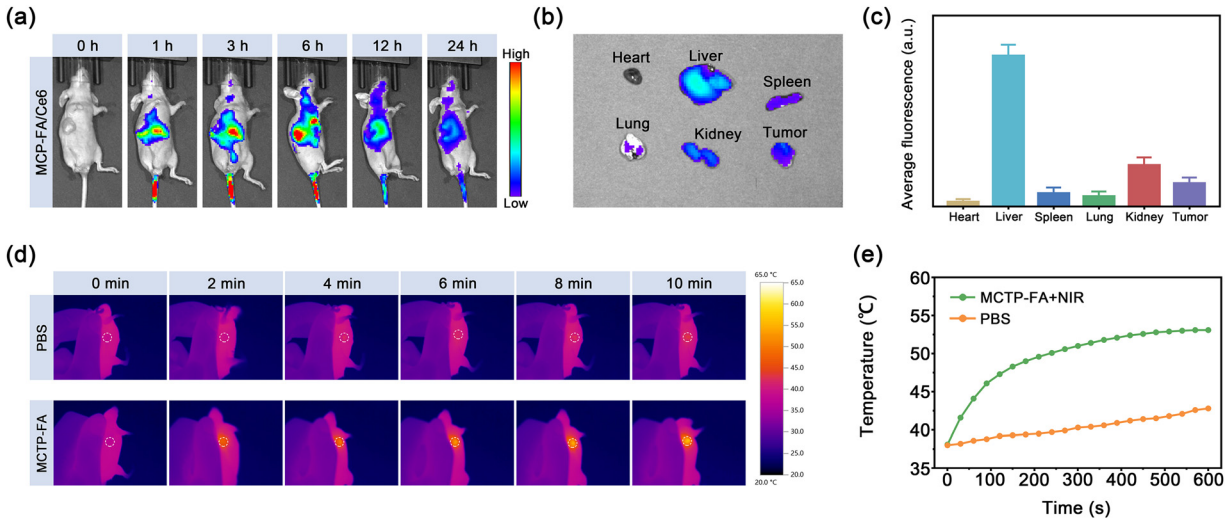

Fig. 5 (a) *In vivo* fluorescence imaging of tumor-bearing mice at the indicated time point after injection of MCP-FA/Ce6 intravenously. (b) *Ex vivo* imaging of major organs and tumor tissues after 24 h post-injection. (c) Semiquantitative analysis of the fluorescence intensity in tumor tissues and major organs. (d) *In vivo* photothermal images and (e) temperature elevating curves of the tumor region at 6 h post-injection of PBS and MCTP-FA with 808 nm laser irradiation (1.0 W cm^{-2}).

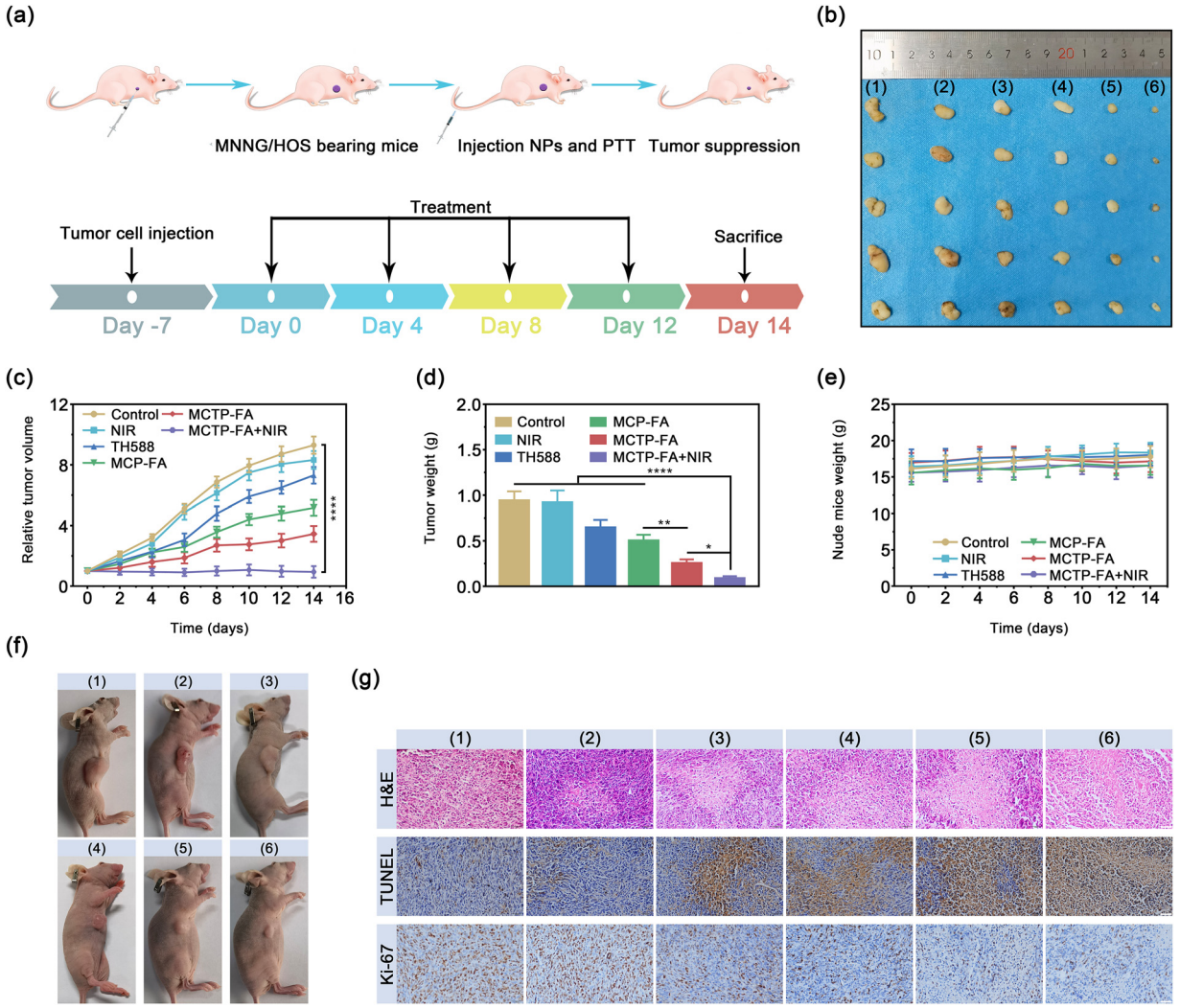

Fig. 6 (a) Schematic diagram of *in vivo* treatment in tumor-bearing mice. (b) Photos of tumors after 14 days of different treatments: (1) control, (2) NIR, (3) TH588, (4) MCP-FA, (5) MCTP-FA, and (6) MCTP-FA + NIR. (c) Relative tumor volume of tumor-bearing mice after 14 days of different treatments. (d) Tumor weights after different treatments for 14 days. (e) Body weight changes of tumor-bearing mice in different groups during treatment. (f) Representative images of tumor-bearing mice after different treatments. (g) H & E, TUNEL and Ki-67 immunohistochemical staining of tumor slices in different groups.

mice in group (6) were exposed to an NIR laser (808 nm, 1.0 W cm^{-2}) for 10 min. The body weight and tumor volume of the mice were monitored every two days during the treatment period. As shown in Fig. 6b–d, no significant tumor inhibition was observed in the NIR treatment group compared to the control, indicating that the tumor growth inhibition effect of NIR irradiation alone was limited. Unsurprisingly, from group 3 onwards, a more sufficient tumor suppressive efficiency was observed with the gradual progress of the sequential catalytic treatment centered on the Fenton-like reaction. Moreover, no significant changes in body weight were observed in each group, indicating negligible systemic toxicity for all treatments in mice (Fig. 6e).

At the end of the treatment, tumor tissues and major organs were collected for histopathological analysis. Consistent with the tendency of tumor suppression in representative mice (Fig. 6f), H & E staining revealed the most pronounced condensed nuclei of cancer cells and typical histopathological damage in the group (6). Moreover, TUNEL staining also confirmed that MCTP-FA + NIR therapy was more likely to lead to tumor *in situ* apoptosis. Additionally, Ki67 immunohistochemistry assays were applied to analyze the proliferation characteristics of tumor cells. As expected, the proliferation capacity of tumor cells treated with MCTP-FA + NIR was significantly inhibited (Fig. 6g). Meanwhile, in view of the powerful antitumor activity of this sequential therapy, we systematically studied the toxic effects of MCTP-FA NPs to guarantee its safe application. As shown in Fig. S18 (ESI†), H & E staining of the major organs showed no obvious tissue damage after various treatments compared with the control group. Meanwhile, hematological analysis also confirmed that MCTP-FA had no noticeable toxicity toward liver and renal functions (Fig. S19, ESI†). All the experimental results validated that the prepared MCTP-FA NPs with excellent biocompatibility and promising anti-tumor efficacy are

expected to become a promising candidate for tumor synergetic therapy.

4. Conclusions

In summary, we successfully achieved the decoration of CeO_2 and the loading of TH588 by using the ideal large mesoporous channels of DMSN, and finally developed a sequential nanotherapeutic platform MCTP-FA for targeted tumor ablation *via* hyperthermia-enhanced POD-mimic activity, GSH consumption as well as inhibiting the MTH1-mediated DNA damage repair pathway. In the slightly acidic TME, depolymerization of PDA shell leads to responsive release of TH588 and exposure of catalytic core CeO_2 NPs. CeO_2 harboring multivalent elements ($Ce^{3+/4+}$) could catalyze H_2O_2 to generate highly toxic $^{\bullet}OH$ in acidic TMEs, as well as eliminate the GSH through redox reaction to relieve the antioxidant capacity of the tumor and further promote the efficacy of CDT, resulting in oxidative damage of guanine in the nucleotide pool. Next, acid-responsive released TH588 could inhibit the MTH1-mediated DNA damage repair pathway, resulting in the accumulation of oxidative damage. Most importantly, the hyperthermia induced by the excellent photothermal conversion capability of MCTP-FA in the NIR region amplified the POD-mimic and GSH consumption activities. Both *in vivo* and *in vitro* experiments have confirmed that the hyperthermia-enhanced nano-catalytic scheme based on a MCTP-FA nanoplatform has a promising antitumor efficacy. Taken together, this novel photothermal enhanced sequential nano-catalytic therapy strategy provides a very promising solution for cancer synergetic therapy.

Author contributions

Qingcheng Song, Yingze Zhang and Hongzhi Hu conceived and designed the research. Yiran Zhang and Haiyue Zhao performed the cell experiments. Xiangtian Deng and Yueyao Zhang performed the *in vivo* experiments. Qingcheng Song completed this manuscript. Wei Chen and Junyong Li gave useful suggestions for this work. All authors read and approved the final manuscript.

Conflicts of interest

The authors declare no conflict of interest.

References

1 L. H. Fu, Y. Wan, C. Qi, J. He, C. Li, C. Yang, H. Xu, J. Lin and P. Huang, *Adv. Mater.*, 2021, **33**, e2006892.
2 Z. Tang, Y. Liu, M. He and W. Bu, *Angew. Chem., Int. Ed.*, 2019, **58**, 946–956.
3 P. Hu, T. Wu, W. Fan, L. Chen, Y. Liu, D. Ni, W. Bu and J. Shi, *Biomaterials*, 2017, **141**, 86–95.
4 M. Valko, D. Leibfritz, J. Moncol, M. Cronin, M. Mazur and J. Telser, *Int. J. Biochem. Cell Biol.*, 2007, **39**, 44–84.
5 L. Feng, R. Xie, C. Wang, S. Gai, F. He, D. Yang, P. Yang and J. Lin, *ACS Nano*, 2018, **12**, 11000–11012.
6 J. Kim, H. R. Cho, H. Jeon, D. Kim, C. Song, N. Lee, S. H. Choi and T. Hyeon, *J. Am. Chem. Soc.*, 2017, **139**, 10992–10995.
7 S. Mura, J. Nicolas and P. Couvreur, *Nat. Mater.*, 2013, **12**, 991–1003.
8 H. R. Burachaloo, F. Karimi, K. Xie, Q. Fu, P. Gurr, D. Dunstan and G. Qiao, *ACS Appl. Mater. Interfaces*, 2017, **9**, 33599–33608.
9 Y. Sun, Z. Wang, P. Zhang, J. Wang, Y. Chen, C. Yin, W. Wang, C. Fan and D. Sun, *Biomater. Sci.*, 2020, **8**, 7154–7165.
10 Y. Ling, M. Long, P. Hu, Y. Chen and J. Huang, *J. Hazard. Mater.*, 2014, **264**, 195–202.
11 Z. Wang and R. Yu, *Adv. Mater.*, 2019, **31**, e1800592.
12 F. Cheng, S. Wang, H. Zheng, S. Yang, L. Zhou, K. Liu, Q. Zhang and H. Zhang, *Colloids Surf., B*, 2021, **205**, 111878.
13 P. Sudarsanam, B. Hillary, B. Mallesham, B. Rao, M. Amin, A. Nafady, A. Alsalme, B. Reddy and S. Bhargava, *Langmuir*, 2016, **32**, 2208–2215.
14 D. Zhang, X. Du, L. Shi and R. Gao, *Dalton Trans.*, 2012, **41**, 14455–14475.
15 D. Tarn, C. Ashley, M. Xue, E. Carnes, J. Zink and C. Brinker, *Acc. Chem. Res.*, 2013, **46**, 792–801.
16 T. Kim, E. Momin, J. Choi, K. Yuan, H. Zaidi, J. Kim, M. Park, N. Lee, M. McMahon, A. Quinones-Hinojosa, J. Bulte, T. Hyeon and A. Gilad, *J. Am. Chem. Soc.*, 2011, **133**, 2955–2961.
17 D. Trachootham, J. Alexandre and P. Huang, *Nat. Rev. Drug Discov.*, 2009, **8**, 579–591.
18 Y. Wang, W. Yin, W. Ke, W. Chen, C. He and Z. Ge, *Biomacromolecules*, 2018, **19**, 1990–1998.
19 K. Murakami, M. Haneda, T. Makino and M. Yoshino, *Food Chem. Toxicol.*, 2007, **45**, 1258–1262.
20 K. Sakumi, M. Furuichi, T. Tsuzuki, T. Kakuma, S. Kawabata, H. Maki and M. Sekiguchi, *J. Biol. Chem.*, 1993, **268**, 23524–23530.
21 J. J. Hu, Y. Chen, Z. H. Li, S. Y. Peng, Y. Sun and X. Z. Zhang, *Nano Lett.*, 2019, **19**, 5568–5576.
22 Y. Nakabeppu, *Int. J. Mol. Sci.*, 2014, **15**, 12543–12557.
23 H. Gad, T. Koolmeister, A.-S. Jemth, S. Eshtad, S. A. Jacques, C. E. Ström, L. M. Svensson, N. Schultz, T. Lundbäck, B. O. Einarsdottir, A. Saleh, C. Göktürk, P. Baranczewski, R. Svensson, R. P. A. Berntsson, R. Gustafsson, K. Strömberg, K. Sanjiv, M.-C. Jacques-Cordonnier, M. Desroses, A.-L. Gustavsson, R. Olofsson, F. Johansson, E. J. Homan, O. Loseva, L. Bräutigam, L. Johansson, A. Höglund, A. Hagenkort, T. Pham, M. Altun, F. Z. Gaugaz, S. Vikingsson, B. Evers, M. Henriksson, K. S. A. Vallin, O. A. Wallner, L. G. J. Hammarström, E. Wiita, I. Almlöf, C. Kalderén, H. Axelsson, T. Djureinovic, J. C. Puigvert, M. Häggblad, F. Jeppsson, U. Martens, C. Lundin, B. Lundgren, I. Granelli, A. J. Jensen, P. Artursson, J. A. Nilsson, P. Stenmark, M. Scobie, U. W. Berglund and T. Helleday, *Nature*, 2014, **508**, 215–221.
24 L. Zhao, J. Li, Y. Su, L. Yang, L. Chen, L. Qiang, Y. Wang, H. Xiang, H. P. Tham, J. Peng and Y. Zhao, *Sci. Adv.*, 2020, **6**, eaaz0575.

25 S. Dong, Y. Dong, T. Jia, S. Liu, J. Liu, D. Yang, F. He, S. Gai, P. Yang and J. Lin, *Adv. Mater.*, 2020, **32**, e2002439.
26 B. Chen, C. Zhang, W. Wang, Z. Chu, Z. Zha, X. He, W. Zhou, T. Liu, H. Wang and H. Qian, *ACS Nano*, 2020, **14**, 14919–14928.
27 X. Zeng, M. Luo, G. Liu, X. Wang, W. Tao, Y. Lin, X. Ji, L. Nie and L. Mei, *Adv. Sci.*, 2018, **5**, 1800510.
28 W. Cheng, X. Zeng, H. Chen, Z. Li, W. Zeng, L. Mei and Y. Zhao, *ACS Nano*, 2019, **13**, 8537–8565.
29 W. Cheng, C. Liang, L. Xu, G. Liu, N. Gao, W. Tao, L. Luo, Y. Zuo, X. Wang, X. Zhang, X. Zeng and L. Mei, *Small*, 2017, **13**, e1700623.
30 S. Gao, H. Lin, H. Zhang, H. Yao, Y. Chen and J. Shi, *Adv. Sci.*, 2019, **6**, 1801733.
31 Y. Lu, L. Li, Z. Lin, M. Li, X. Hu, Y. Zhang, M. Peng, H. Xia and G. Han, *Adv. Healthc. Mater.*, 2018, **7**, e1800602.
32 R. Zhang, S. Su, K. Hu, L. Shao, X. Deng, W. Sheng and Y. Wu, *Nanoscale*, 2015, **7**, 19722–19731.
33 C. Chen, W. Tang, D. Jiang, G. Yang, X. Wang, L. Zhou, W. Zhang and P. Wang, *Nanoscale*, 2019, **11**, 11012–11024.
34 W. Shi, Q. Wang, Y. Long, Z. Cheng, S. Chen, H. Zheng and Y. Huang, *Chem. Commun.*, 2011, **47**, 6695–6697.
35 M. Huo, L. Wang, Y. Chen and J. Shi, *Nat. Commun.*, 2017, **8**, 357.
36 B. Jiang, D. Duan, L. Gao, M. Zhou, K. Fan, Y. Tang, J. Xi, Y. Bi, Z. Tong, G. Gao, N. Xie, A. Tang, G. Nie, M. Liang and X. Yan, *Nat. Protoc.*, 2018, **13**, 1506–1520.
37 H. J. Liu, M. Wang, X. Hu, S. Shi and P. Xu, *Small*, 2020, **16**, e2003398.
38 F. Novio, *Molecules*, 2020, **25**, 3449.
39 J. W. Ai, B. Liu and W. D. Liu, *Mater. Sci. Eng., C*, 2017, **76**, 1181–1187.
40 L. S. Lin, J. Song, L. Song, K. Ke, Y. Liu, Z. Zhou, Z. Shen, J. Li, Z. Yang, W. Tang, G. Niu, H. H. Yang and X. Chen, *Angew. Chem., Int. Ed.*, 2018, **57**, 4902–4906.
41 W. Guo, Y. An, L. Jiang, C. Geng and L. Zhong, *Phytother. Res.*, 2010, **24**, 352–359.
42 K. Murakami, M. Haneda, T. Makino and M. Yoshino, *Food Chem. Toxicol.*, 2007, **45**, 1258–1262.
43 C. C. Tsai, S. B. Wu, C. Y. Cheng, S. S. Kao, H. C. Kau, S. H. Chiou, W. M. Hsu and Y. H. Wei, *Eye*, 2010, **24**, 1520–1525.
44 Y. Cheng, X. Kong, Y. Chang, Y. Feng, R. Zheng, X. Wu, K. Xu, X. Gao and H. Zhang, *Adv. Mater.*, 2020, **32**, e1908109.
45 L. Wang, X. Niu, Q. Song, J. Jia, Y. Hao, C. Zheng, K. Ding, H. Xiao, X. Liu, Z. Zhang and Y. Zhang, *J. Controlled Release*, 2020, **318**, 197–209.
46 S. Javadov, S. Jang, X. Chapa-Dubocq, Z. Khuchua and A. Camara, *J. Mol. Med.*, 2021, **99**, 57–73.
47 J. Molina, Y. Sun, M. Protopopova, S. Gera, M. Bandi, C. Bristow, T. McAfoos, P. Morlacchi, J. Ackroyd, A. Agip, G. Al-Atrash, J. Asara, J. Bardenhagen, C. Carrillo, C. Carroll, E. Chang, S. Ciurea, J. Cross, B. Czako, A. Deem, N. Daver, J. de Groot, J. Dong, N. Feng, G. Gao, J. Gay, M. Do, J. Greer, V. Giuliani, J. Han, L. Han, V. Henry, J. Hirst, S. Huang, Y. Jiang, Z. Kang, T. Khor, S. Konoplev, Y. Lin, G. Liu, A. Lodi, T. Lofton, H. Ma, M. Mahendra, P. Matre, R. Mullinax, M. Peoples, A. Petrocchi, J. Rodriguez-Canale, R. Serreli, T. Shi, M. Smith, Y. Tabe, J. Theroff, S. Tiziani, Q. Xu, Q. Zhang, F. Muller, R. DePinho, C. Toniatti, G. Draetta, T. Heffernan, M. Konopleva, P. Jones, M. Di Francesco and J. Marszalek, *Nat. Med.*, 2018, **24**, 1036–1046.

